J Mater Sci (2018) 53:14447–14455

Electronic materials

Field effect properties of single-layer $MoS_{2(1-x)}Se_{2x}$ nanosheets produced by a one-step CVD process

Dengxuan Tang[1], Fang Wang[1,*], Baijun Zhang[1], Yi Li[1], Yue Li[1], Yulin Feng[2], Yemei Han[1], Jun Ma[1], Tianling Ren[3], and Kailiang Zhang[1,*]

[1] School of Electrical and Electronic Engineering, Tianjin Key Laboratory of Film Electronic and Communication Devices, Tianjin University of Technology, Tianjin 300384, China

[2] Institute of Microelectronics, Peking University, Beijing 100871, China

[3] Tsinghua National Laboratory for Information Science and Technology, Institute of Microelectronics, Tsinghua University, Beijing 100084, China

Received: 10 May 2018
Accepted: 18 June 2018
Published online: 10 July 2018

ABSTRACT

In recent years, interfacial doping with other atoms, molecules, and nanoparticles in molybdenum disulfide (MoS_2) has been proven as a new route to explore the potential application of 2D materials in microelectronical devices. In this paper, we utilized a one-step chemical vapor deposition approach to synthesize monolayer $MoS_{2(1-x)}Se_{2x}$ nanosheets in atmospheric pressure using MoO_3, S, and Se powders as precursors. AFM and visible-light microscopy showed that the as-grown nanosheets were single layers, their surface was atomic flat, and the maximum grain size was over 100 μm. XPS characterization demonstrated that the concentration of selenium in $MoS_{2(1-x)}Se_{2x}$ nanosheets was affected by the amount of selenium powder in the doping process. The back-gate FETs were fabricated to investigate the electrical properties of monolayer $MoS_{2(1-x)}Se_{2x}$ nanosheets with different Se contents. The field effect properties of $MoS_{2(1-x)}Se_{2x}$ (x = 0.65) transistors indicated that a moderate mobility was achieved, and ohmic contact was obtained at the interface of the $MoS_{2(1-x)}Se_{2x}$ channel and metal electrodes. Characterization using high-resolution transmission electron microscopy showed that the microstructure of as-grown $MoS_{2(1-x)}Se_{2x}$ (x = 0.65) had a regular hexagonal lattice structure, which revealed that it was a single-crystalline two-dimensional material.

Introduction

As a member of two-dimensional transition metal dichalcogenides (TMDs) [1, 2], molybdenum disulfide (MoS_2) has been widely studied due to its unique material properties [3–6]. Unlike graphene, which has no bandgap, molybdenum disulfide is a semiconductor and its bandgaps are around 1.2–1.8 eV depending on the number of layers. When MoS_2 is decreased from few layers to a single layer (around 0.65 nm), MoS_2 will change from an indirect semiconductor to a direct

Address correspondence to E-mail: fwang75@163.com; kailiang_zhang@163.com

https://doi.org/10.1007/s10853-018-2617-5

semiconductor [7, 8]. Due to its outstanding physical and chemical properties, MoS_2 has great prospects in the fields of microelectronics [9, 10], optoelectronics [11, 12], and energy storage [13–15]. In order to achieve the desired physical and chemical properties of MoS_2, some progress has been made in experimental and theoretical calculation of molybdenum disulfide doping [16–19]. Dolui et al. investigated the impact of substituted elements on the characteristics of MoS_2 by first-principles calculations [19]. Other studies have reported that the bandgap was clearly modulated when substituted elements such as Se or W were introduced during the preparations of MoS_2 [20–23]. However, there are still many major challenges in preparing the $MoS_{2(1-x)}Se_{2x}$ alloy. For example, it is still hard to synthesize large-area and layer-controlled $MoS_{2(1-x)}Se_{2x}$ nanosheets. The effect of the Se/S source ratio on the concentration and uniformity of substituted selenium in the samples has not been fully investigated. In addition, the performance of electrical devices fabricated by $MoS_{2(1-x)}Se_{2x}$ is still not optimal.

Here, we reported the synthesis of large-area $MoS_{2(1-x)}Se_{2x}$ monolayers by one-step atmospheric pressure chemical vapor deposition (APCVD). During the preparation process, the ratio of selenium and sulfur source not only determined the elemental composition of the samples, but also affected the grain size of the $MoS_{2(1-x)}Se_{2x}$ monolayers. The content and distribution of selenium in the triangular $MoS_{2(1-x)}Se_{2x}$ domains were characterized by XPS and EDX spectra. The central positions and intensities of Raman peaks corresponding to $MoS_{2(1-x)}Se_{2x}$ nanosheets with different Se contents clearly demonstrated variation of vibration modes in the alloy. High-resolution transmission electron microscopy (HRTEM) images demonstrated that as-grown samples were single crystals. To measure the electrical properties, synthesized $MoS_{2(1-x)}Se_{2x}$ nanosheets were used as channels in field effect transistors. With different Se content, these exquisite devices showed promising electrical performances. Our research provides the possibility for the application of $MoS_{2(1-x)}Se_{2x}$ in the micro–nano-electronic field.

Results and discussion

$MoS_{2(1-x)}Se_{2x}$ nanosheets were grown on SiO_2/Si substrates, using a three-temperature-zone tube furnace (Fig. 1a). Due to the different melting points, selenium powders and sulfur powders were placed separately in different upstream regions. During the experiment, sulfur and selenium vapor reacted with MoO_3 after being transported by the carrier gas in downstream zone III to where the substrates were located. Here, the carrier gas was a mixture gas of hydrogen and argon (8% H_2). As a reduction agent, the introduced H_2 could convert MoO_3 to MoO_{3-x}, which facilitated the further reaction (see Supporting Information (SI): SI-1).

The images from the visible-light microscope in Fig. 1b–f showed the isolated triangular domains of $MoS_{2(1-x)}Se_{2x}$ nanosheets, which ranged in size from a few microns to more than 100 μm. The grain size of the samples was closely related to the ratio of selenium and sulfur powders. The total amount of selenium and sulfur powders used in the experiments was 20 mg. As the ratio of selenium powder increased, the size of $MoS_{2(1-x)}Se_{2x}$ triangular domains clearly decreased (Fig. 1b–f). The major reason for this phenomenon is that the chemical activity of sulfur is stronger than selenium, and thus crystallization of the $MoS_{2(1-x)}Se_{2x}$ nanosheets is more difficult at the Se-rich reaction process compared to the S-rich atmosphere [24–26]. Topography of $MoS_{2(1-x)}Se_{2x}$ nanosheets was characterized by an atomic force microscope (AFM). The triangular domain in Fig. 1g had a homogenous contrast and no obvious particles, which revealed that the surface of the prepared sample was clean and atomic flat. The white curve in Fig. 1g was the cross-sectional scan of the sample (marked by a red line), and its height was ~ 0.8 nm, indicating that the $MoS_{2(1-x)}Se_{2x}$ nanosheet was a single layer [27]. In the process of $MoS_{2(1-x)}Se_{2x}$ growth, the amount of hydrogen flow was the main factor to obtain these monolayer samples (see SI: Fig. S1 and Fig. S2).

The chemical states and Se contents in $MoS_{2(1-x)}Se_{2x}$ nanosheets were confirmed by X-ray photoelectron spectroscopy (XPS). Figure 2a showed that the S 2p had two peaks at ~ 162.8 and ~ 164.0 eV, which were attributed to S $2p^{3/2}$ and S $2p^{1/2}$, respectively. The binding energy of Se $3p^{3/2}$ was observed at ~ 161.2 eV. According to the above-mentioned results, x in $MoS_{2(1-x)}Se_{2x}$ could be calculated by the following formula:

$$S/Se = (I_s \times F_{Se})/(I_{Se} \times F_S) \quad (1)$$

where I_S and I_{Se} were the areas under the peaks of S $2p^{3/2}$ and Se $3p^{3/2}$, respectively; and F_S and F_{Se}

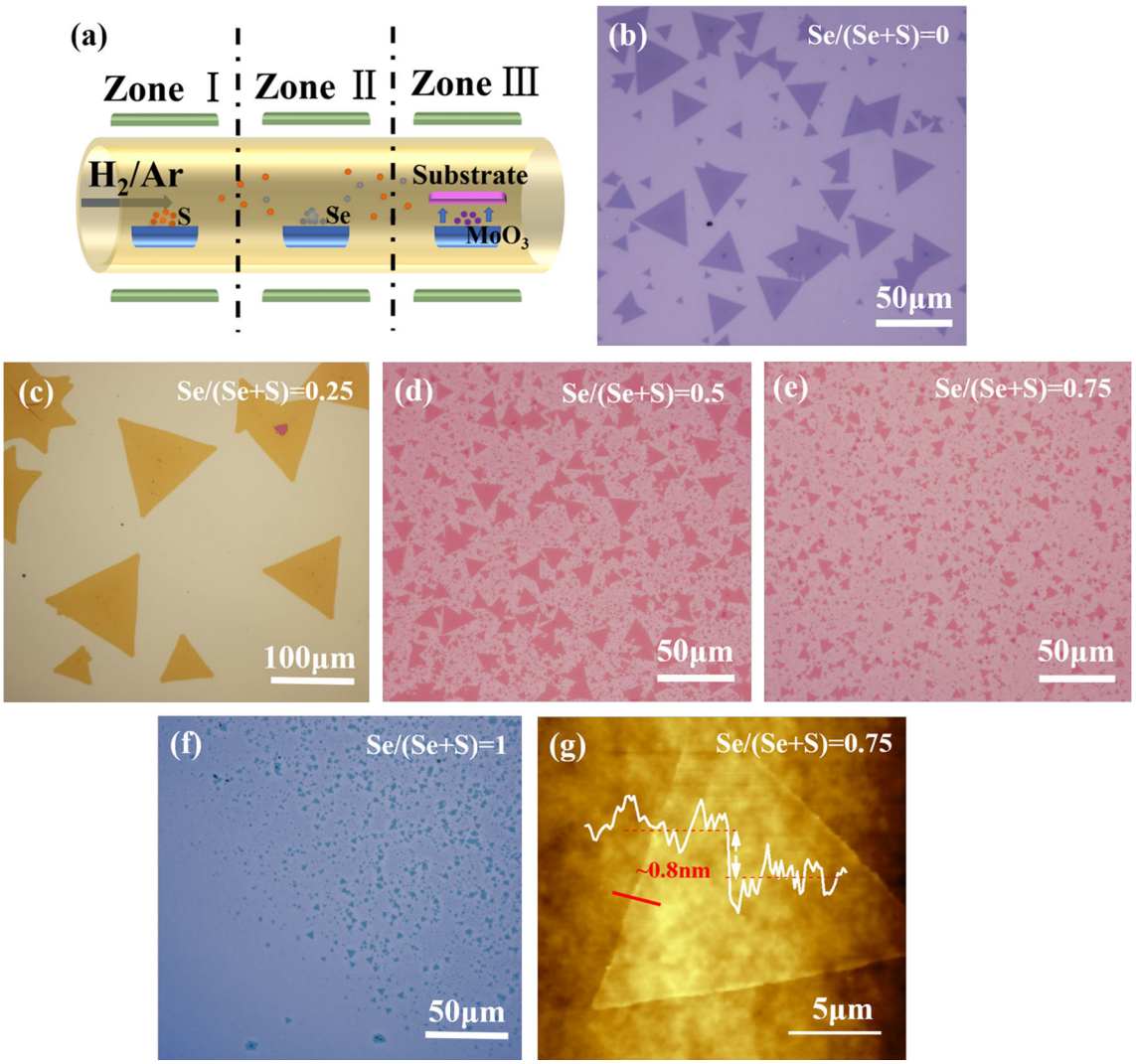

Figure 1 **a** Schematic illustration for the growth of monolayer $MoS_{2(1-x)}Se_{2x}$ nanosheets. **b**–**f** Visible-light microscope images of as-grown $MoS_{2(1-x)}Se_{2x}$ nanosheets with different ratios of selenium and sulfur powders. **g** AFM images of monolayer triangular $MoS_{2(1-x)}Se_{2x}$ nanosheets.

represented the relative symmetric factors for S $2p^{3/2}$ (0.4453) and Se $3p^{3/2}$ (0.8493), respectively [28]. It was notable that x in $MoS_{2(1-x)}Se_{2x}$ went up as the ratio of selenium powders rose during the experiments (Fig. 2b). With increase in the Se content in $MoS_{2(1-x)}Se_{2x}$ nanosheets, the peak of Se $3p^{3/2}$ was obvious, while the intensities of S $2p^{3/2}$ and $2p^{1/2}$ became weak and begin to disappear. The peaks at ~ 229.7 and ~ 232.8 eV corresponded to Mo^{4+} $3d^{5/2}$ and Mo^{4+} $3d^{3/2}$, respectively (Fig. 2c), in agreement with previously reported values [7]. There was no obvious peak of Mo^{6+} $3d^{5/2}$ at ~ 236 eV, indicating that MoO_3 was completely reduced to $MoS_{2(1-x)}Se_{2x}$. The doublet peaks of Se $3d^{5/2}$ and Se $3d^{3/2}$ were evident at ~ 55.2 and ~ 56.1 eV, as long as selenium was contained in the nanosheets (Fig. 2d) [29].

Raman spectroscopy was an effective method to analyze the phonon vibration mode properties of the TMDs. While $MoS_{2(1-x)}Se_{2x}$ was produced from APCVD, the two sets of composition-dependent peaks were obtained in the Raman spectra [30], corresponding to an $MoSe_2$-related feature at low frequency (200–300 cm^{-1}) and an MoS_2 typical feature at high frequency (350–410 cm^{-1}) (Fig. 3a). There were two typical peaks of MoS_2 centered at ~ 401.1 cm^{-1} (E^1_{2g}) and ~ 380.5 cm^{-1}(A_{1g}), which were attributed to in-plane vibration of S atoms and out-of-plane vibration of S and Mo atoms, respectively. The inset in Fig. 3b showed the schematic of

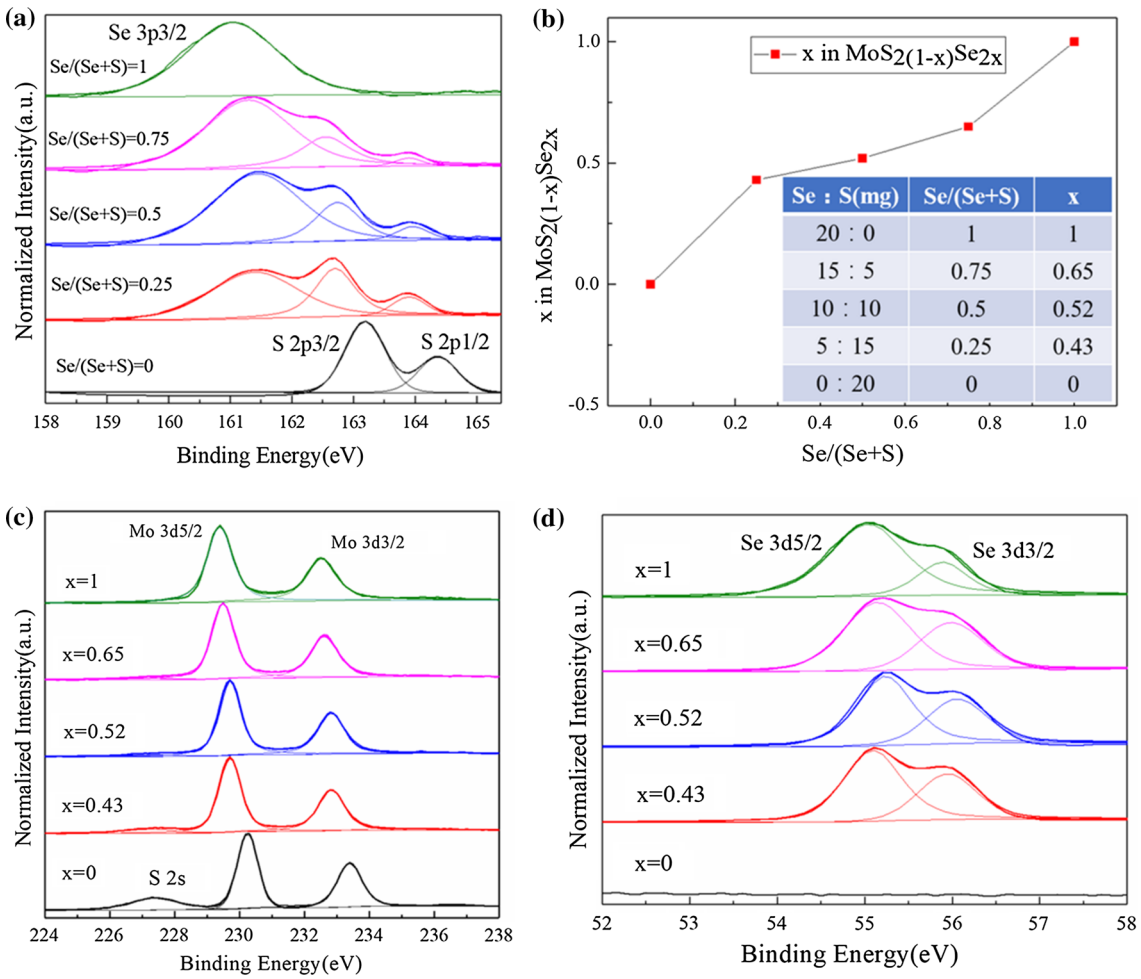

Figure 2 XPS spectra of $MoS_{2(1-x)}Se_{2x}$ monolayers. **a** 158–165 eV binding energy stage. **b** The curve of the x value in $MoS_{2(1-x)}Se_{2x}$ with the amount of selenium sources. **c** 224–238 eV binding energy stage. **d** 52–58 eV binding energy stage.

two vibration modes. These MoS_2-like modes shifted to low frequency by increasing the Se content in $MoS_{2(1-x)}Se_{2x}$. This result suggested that the introduction of Se atoms distorted the Mo-S bonds and softened the vibrations of E^1_{2g} and A_{1g} modes of MoS_2. As the Se atoms occupied the parts of sulfur sites, $MoSe_2$-like peaks of monolayer $MoS_{2(1-x)}Se_{2x}$ appeared and became noticeable between 200 and

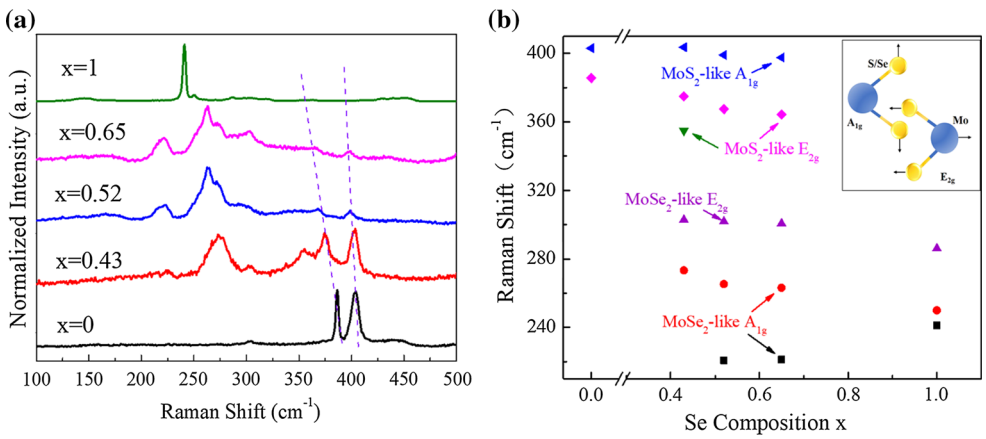

Figure 3 **a** Raman spectra of $MoS_{2(1-x)}Se_{2x}$ monolayers. **b** Plots of Raman shifts along with Se composition x in $MoS_{2(1-x)}Se_{2x}$ monolayer (inset is the schematic of A_{1g} and E^1_{2g} modes).

300 cm^{-1}. When selenium was completely substituted for sulfur, the out-of-plane A_{1g} mode of $MoSe_2$ was identified at 241.1 cm^{-1}.

The field effect transistors (FETs) were fabricated by electron beam lithography (EBL) to demonstrate the electrical properties of the synthesized $MoS_{2(1-x)}Se_{2x}$ monolayers with different Se contents (x = 0, 0.43, 0.65). 10 nm Ti and 100 nm Au were deposited as the electrodes of FETs by electron beam evaporation and magnetron sputtering, respectively. The $I_{ds}-V_{gs}$ transfer characteristic curves (Fig. 4a, c, e) suggested that all the $MoS_{2(1-x)}Se_{2x}$ devices exhibited n-type transport behavior. The high I_{on}/I_{off} ratios of $\sim 10^7$ were extracted from semilogarithmic coordinates in the inset shown in Fig. 4a, c, e. Carrier mobility μ was calculated by the following formula: [3, 31]

$$\mu = \left[dI_{ds}/dV_{gs}\right] \times \left[L/(WC_{ox}V_{ds})\right] \quad (2)$$

where L and W were channel length of 2 μm and width of 1 μm, respectively; and C_{ox} was the SiO_2 gate capacitance, which was estimated to be approximately 1.16×10^{-8} Fcm^{-2}. As Se contents rose from x = 0 to x = 0.65, carrier mobility of devices gradually improved from $\sim$ 0.12 to $\sim$ 3.72 cm^2 V^{-1} s^{-1}. The much lower carrier mobility of x = 0 and x = 0.43 was possibly attributed to the following reasons: first, poor contact existed between $MoS_{2(1-x)}Se_{2x}$ channels and the Au electrodes, causing serious contact resistance. Second, introduced Se caused inevitable lattice distortion or defects in the $MoS_{2(1-x)}Se_{2x}$ samples reducing the efficiency of carrier transport. Third, organic or inorganic impurity derived from the process of fabricating and testing FETs might have resulted in the degradation of device performance. The contact between the channel and electrodes could be characterized by $I_{ds}-V_{ds}$ curves (Fig. 4b, d, f). The contact of x = 0 and x = 0.43 belonged to the Schottky contact (Fig. 4b, d), but when x = 0.65, the linear curves in Fig. 4f indicated that ohmic contact was formed between the $MoS_{2(1-x)}Se_{2x}$ channel and the Au electrodes. The ohmic contact improved the transport of carrier mobility in monolayer $MoS_{2(1-x)}Se_{2x}$ (x = 0.65) FETs. Another reason for obtaining the best electrical properties in x = 0.65 samples was that the bandgap of $MoS_{2(1-x)}Se_{2x}$ decreased with the rise in selenium contents [32], which made it easier for carriers to be

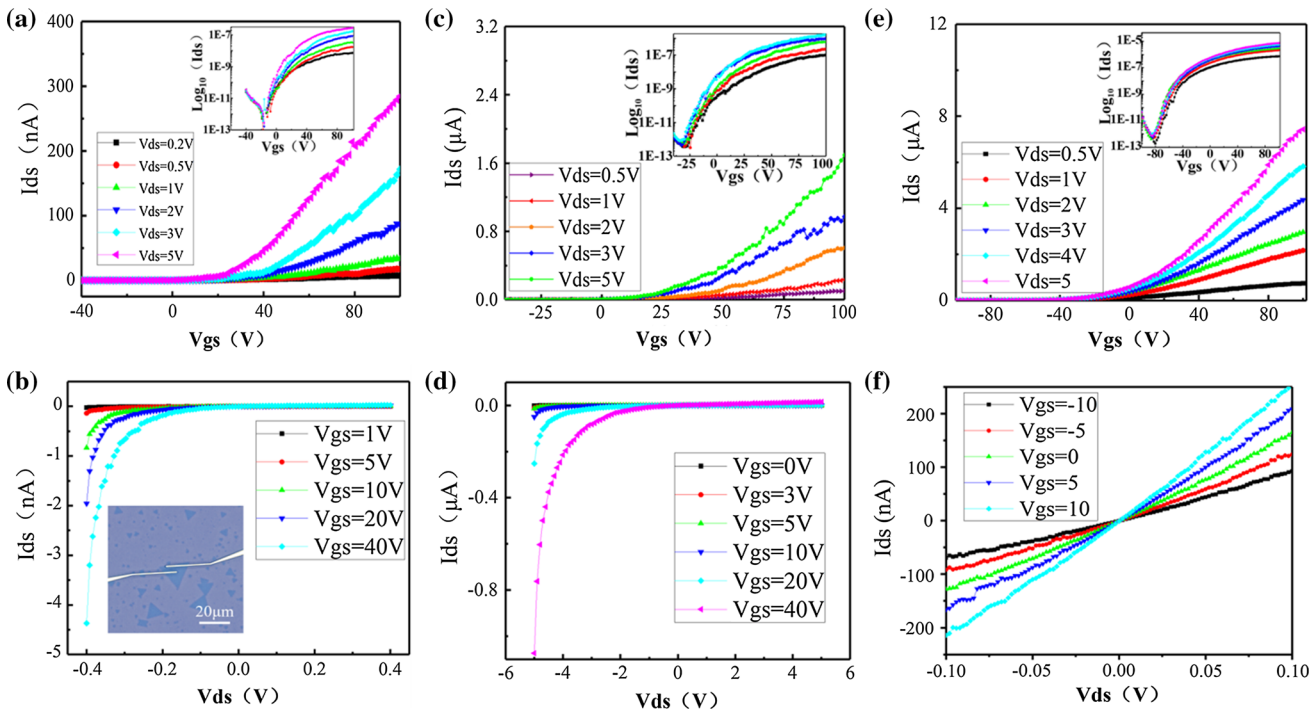

Figure 4 **a**, **c**, **e** The source-drain current to the gate voltage ($I_{ds}-V_{gs}$) and **b**, **d**, **f** the source-drain current to the source-drain voltage ($I_{ds}-V_{ds}$) for FETs in which the $MoS_{2(1-x)}Se_{2x}$ nanosheets were used as channels. **a**, **b** for x = 0; **c**, **d** for x = 0.43; **e**, **f** for x = 0.65. The insets of **a**, **c**, **e** were semilogarithmic coordinates of $I_{ds}-V_{gs}$ curves and the inset of **b** was the visible-light microscope image of the FETs.

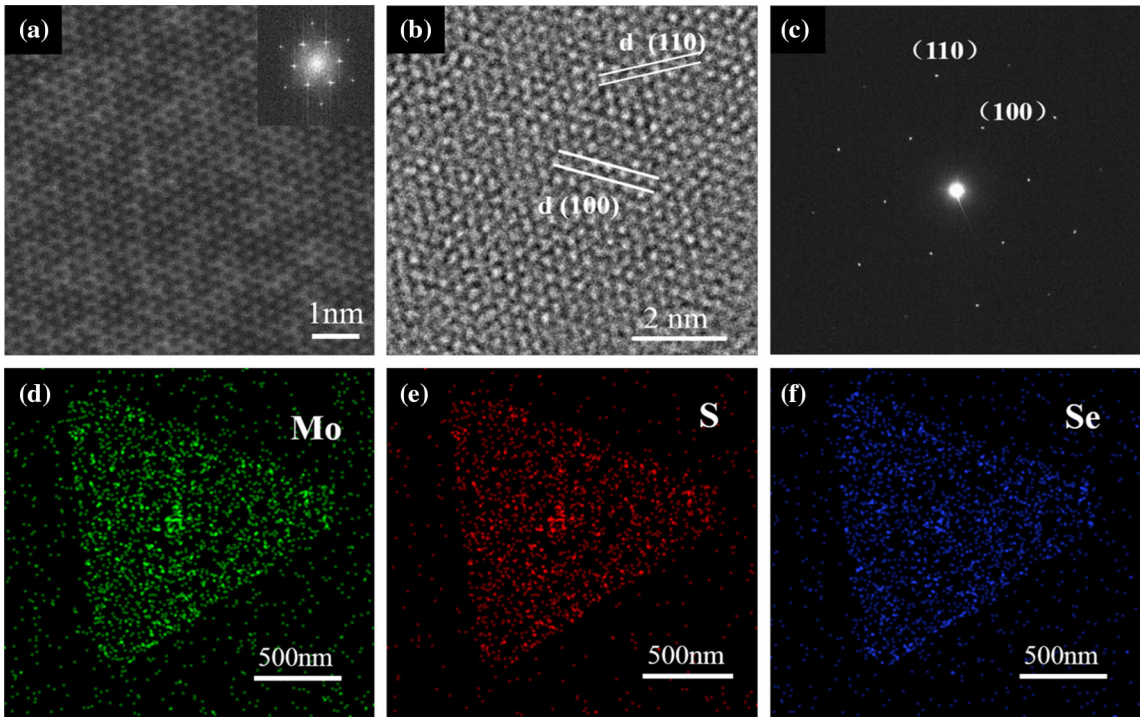

Figure 5 **a** HAADF-STEM image of the $MoS_{2(1-x)}Se_{2x}$ nanosheet ($x = 0.65$). **b** High-resolution TEM images of the $MoS_{2(1-x)}Se_{2x}$ nanosheet ($x = 0.65$). **c** The bright spots in selected area electron diffraction (SAED) pattern reveal that the sample is a single crystal. EDX mappings of **d** Mo, **e** S and **f** Se in the $MoS_{2(1-x)}Se_{2x}$ nanosheet.

exciting from the top of the valence band to the conduction band, thus improving the electrical properties. To further promote the performance of monolayer $MoS_{2(1-x)}Se_{2x}$ FETs, elaborating the high-k top-gating [33] and tuning the contact between channels and electrodes [34] should be considered in future research.

In order to further explore the microstructure of the monolayer $MoS_{2(1-x)}Se_{2x}$ nanosheets ($x = 0.65$) with optimal electrical properties, transmission electron microscopy (TEM) combined with energy-dispersive X-ray spectroscopy (EDX) was conducted to investigate its lattice structure and element distribution. In the image of atomic-resolution high-angle annular dark-field (HAADF) scanning transmission electron microscopy (STEM) (Fig. 5a), different atoms could be identified by Z contrast (Z = atomic number) [20]. The Mo sites were brighter than most bi-chalcogen (X_2, X = S, Se) sites because the atomic number of Mo (42) was larger than those of Se (34) and S (16). Figure 5a revealed that Se existed in the lattice of MoS_2 in the form of substitution doping. Two predominant lattice spacings measured from the high-resolution TEM image (Fig. 5b) were ~ 0.28 nm and ~ 0.16 nm, representing (100) and (110) planes, respectively [35, 36]. This result was consistent with selected area electron diffraction (SAED) patterns (Fig. 5c) which confirmed that the sample was the single crystal of a hexagonal structure [37]. EDX mapping was used to characterize the distribution of the elements in the samples (and EDX spectrum of $MoS_{2(1-x)}Se_{2x}$ could be seen in SI: Fig. S3). The identical and similar triangles of Fig. 5d–f indicated the ideal element uniformity in the as-grown $MoS_{2(1-x)}Se_{2x}$ monolayer. Combined with images of high-resolution TEM and EDX mapping, $x = 0.65$ of samples had no fatal defects in the lattice arrangement, and the distribution of elements in single samples was homogeneous. Single-crystalline microstructures were important reasons that $MoS_{2(1-x)}Se_{2x}$ ($x = 0.65$) could obtain distinctive electrical properties.

Conclusion

To summarize, we have synthesized the triangular and uniform domains of $MoS_{2(1-x)}Se_{2x}$ monolayer nanosheets by a simple APCVD approach. The impact of the ratio of selenium and sulfur powder on the size and Se contents of $MoS_{2(1-x)}Se_{2x}$ was

investigated in detail. XPS confirmed that the Se contents in $MoS_{2(1-x)}Se_{2x}$ nanosheets increased with increasing selenium powders. The electrical properties of the samples with different selenium contents were also discussed in this paper. The results showed that optimal electrical properties were obtained when the Se concentration of the nanosheets reached the maximum (x = 0.65). According to the microstructure of $MoS_{2(1-x)}Se_{2x}$ (x = 0.65), HRTEM combined with EDX showed that the as-grown nanosheets were single crystals and the distribution of Mo, S and Se was uniform in the triangular domain. This work provides a feasible and convenient method to synthesize high-quality and large-area $MoS_{2(2-x)}Se_{2x}$ monolayers with controllable stoichiometry.

Experimental details

Growth of monolayer $MoS_{2(1-x)}Se_{2x}$ nanosheets

$MoS_{2(1-x)}Se_{2x}$ nanosheets were grown on SiO_2/Si substrates, utilizing a three-temperature-zone tube furnace. Sulfur and selenium powders were placed in upstream zone I (150 °C) and zone II (300 °C), respectively, due to their different melting points; the total amount of selenium and sulfur powders was 20 mg. Silicon oxide substrates were immersed in acetone and isopropanol for ultrasonic cleaning for 10 min as pretreatment. SiO_2 substrates dried by nitrogen were placed face down on ceramic boats with 10 mg MoO_3 powder in downstream zone III. The growth temperature of $MoS_{2(1-x)}Se_{2x}$ in zone III was about 700 °C to 800 °C. The carrier gas was a mixture of argon–hydrogen (8% H_2) gas with 65 sccm during growth.

Characterizations of monolayer $MoS_{2(1-x)}Se_{2x}$ nanosheets

The topography and thickness of as-grown $MoS_{2(1-x)}Se_{2x}$ nanosheets were characterized by visible-light microscopy (Olympus) and atomic force microscopy (AFM, 5600LS). X-ray photoelectron spectroscopy (XPS, Thermo Scientific Escalab 250Xi) was performed with a monochromatic Al Kα X-ray source to investigate the elemental composition of the $MoS_{2(1-x)}Se_{2x}$ nanosheets. The phonon vibration mode properties of $MoS_{2(1-x)}Se_{2x}$ were characterized by Raman spectrum (ThermoFisher DXR) at 532 nm excitation wavelength. HAADF-STEM (Titan Cubed Themis G2 300) was used to identify the atomic phase of $MoS_{2(1-x)}Se_{2x}$ nanosheets at 100 keV. High-resolution transmission electron microscopy combined with EDX spectrum (Talos F200X) was applied at 200 keV to characterize the crystalline structure of the $MoS_{2(1-x)}Se_{2x}$ nanosheets.

Fabrication and characterization of $MoS_{2(1-x)}Se_{2x}$ FETs

The source and drain electrodes of the monolayer $MoS_{2(1-x)}Se_{2x}$ FETs were fabricated by electron beam lithography. The electrode materials were 10 nm Ti and 100 nm Au deposited by electron beam evaporation and magnetron sputtering deposition, respectively. The back-gate electrodes were fabricated by etching p^{++} SiO_2 substrates with BOE solution. The electrical properties of the FETs were measured using a semiconductor parameter analyzer (Agilent B1500A).

Acknowledgements

This work was supported by the National Key Research and Development Program of China (Grant No. 2017YFB0405600), Natural Science Foundation of Tianjin City (Grant Nos. 18JCZDJC30500, 17JCYBJC16100, and 17JCZDJC31700), and National Natural Science Foundation of China (Grant Nos. 61404091, 61274113, 61505144, 51502203, and 51502204).

Compliance with ethical standards

Conflict of interest The authors declare that they have no conflict of interest.

Electronic supplementary material: The online version of this article (https://doi.org/10.1007/s10853-018-2617-5) contains supplementary material, which is available to authorized users.

References

[1] Zheng B, Wang Z, Qi F et al (2017) CVD growth of large-area and high-quality HfS_2 nanoforest on diverse substrates. Appl Surf Sci 435:563–567

[2] Hu P, Wang L, Yoon M et al (2013) Highly responsive ultrathin GaS nanosheet photodetectors on rigid and flexible substrates. Nano Lett 13:1649–1654

[3] Radisavljevic B, Radenovic A, Brivio J, Giacometti V, Kis A (2011) Single-layer MoS_2 transistors. Nat Nanotechnol 6:147–150

[4] Cain JD, Shi F, Wu J, Dravid VP (2016) Growth mechanism of transition metal dichalcogenide monolayers: the role of self-seeding fullerene nuclei. ACS Nano 10:5440

[5] Ling X, Lee Y, Lin Y, Fang W, Yu L, Dresselhaus M, Kong J (2014) Role of the seeding promoter in MoS_2 growth by chemical vapor deposition. Nano Lett 14:464–472

[6] Antonelou A, Sygellou GL, Leftheriotis G, Dracopoulos V, Yannopoulos SN (2016) Facile, substrate-scale growth of mono- and few-layer homogeneous MoS_2 films on Mo foils with enhanced catalytic activity as counter electrodes in DSSCs. Nanotechnology 27:045404

[7] Eda G, Yamaguchi H, Voiry D, Fujita T, Chen M, Chhowalla M (2011) Photoluminescence from chemically exfoliated MoS_2. Nano Lett 11:5111

[8] Feng Y, Zhang K, Wang F et al (2015) Synthesis of large-area highly crystalline monolayer molybdenum disulfide with tunable grain size in a H_2 atmosphere. ACS Appl Mater Inter 7:22587–22593

[9] Desai SB, Madhvapathy SR, Sachid AB et al (2016) MoS_2 transistors with 1-nanometer gate lengths. Science 354:99–102

[10] Radisavljevic B, Whitwick MB, Kis A (2012) Small-signal amplifier based on single-layer MoS_2. Appl Phys Lett 101:66

[11] Tsai DS, Liu KK, Lien DH et al (2013) Few-layer MoS_2 with high broadband photogain and fast optical switching for use in harsh environments. ACS Nano 7:3905–3911

[12] Chen X, Yang H, Liu G et al (2018) Hollow spherical nanoshell arrays of 2D layered semiconductor for high-performance photodetector device. Adv Funct Mater 28:1705153

[13] Chhetri M, Gupta U, Yadgarov L, Rosentsveig R, Tennec R, Rao CNR (2015) Beneficial effect of Re doping on the electrochemical HER activity of MoS_2 fullerenes. Dalton Trans 44:16399

[14] Cao X, Shi Y, Shi W, Rui X, Yan Q, Kong J, Zhang H (2013) Preparation of MoS_2-coated three-dimensional graphene networks for high-performance anode material in lithium-ion batteries. Small 9:3433–3438

[15] Wang Z, Li Q, Xu H et al (2018) Controllable etching of MoS_2 basal planes for enhanced hydrogen evolution through the formation of active edge sites. Nano Energy 49:634–643

[16] Du Y, Liu H, Neal AT, Si M, Ye PD (2013) Molecular doping of multilayer MoS_2 field-effect transistors: reduction in sheet and contact resistances. IEEE Electron Device Lett 34:1328–1330

[17] Fang H, Tosun M, Seol G, Chang TC, Takei K, Guo J, Javey A (2013) Degenerate n-doping of few-layer transition metal dichalcogenides by potassium. Nano Lett 13:1991–1995

[18] Eshun K, Xiong HD, Yu S, Li Q (2015) Doping induces large variation in the electrical properties of MoS_2 monolayers. Solid State Electron 106:44–49

[19] Dolui K, Rungger I, Pemmaraju CD, Sanvito S (2013) Possible doping strategies for MoS_2 monolayers: an ab initio study. Phys Rev B 88:4192–4198

[20] Feng Q, Zhu Y, Hong J et al (2014) Growth of large-area 2D $MoS_{2(1-x)}Se_{2x}$ semiconductor alloys. Adv Mater 26:2648–2653

[21] Zhang W, Li X, Jiang T, Song J, Lin Y, Zhu L, Xu X (2015) CVD synthesis of $Mo_{(1-x)}W_xS_2$ and $MoS_{2(1-x)}Se_{2x}$ alloy monolayers aimed at tuning the bandgap of molybdenum disulfide. Nanoscale 7:13554–13560

[22] Mann J, Ma Q, Odenthal PM et al (2014) 2-Dimensional transition metal dichalcogenides with tunable direct band gaps: $MoS_{2(1-x)}Se_{2x}$ monolayers. Adv Mater 26:1399–1404

[23] Li H, Zhang Q, Duan X et al (2015) Lateral growth of composition graded atomic layer $MoS_{2(1-x)}Se_{2x}$ nanosheets. J Am Chem Soc 137:5284–5287

[24] Lu X, Utama MIB, Lin J et al (2014) Large-area synthesis of monolayer and few-layer $MoSe_2$ films on SiO_2 substrates. Nano Lett 14:2419

[25] Li Y, Zhang K, Wang F, Feng Y, Li Y, Han Y, Tang D, Zhang B (2017) Scalable synthesis of highly crystalline $MoSe_2$ and its ambipolar behavior. ACS Appl Mater Inter 9:36009–36016

[26] Huang JK, Pu J, Hsu CL et al (2014) Large-area synthesis of highly crystalline WSe_2 monolayers and device applications. ACS Nano 8:923–930

[27] Feng Q, Mao N, Wu J, Xu H, Wang C, Zhang J, Xie L (2015) Growth of $MoS_{2(1-x)}Se_{2x}$ (x = 0.41–1.00) monolayer alloys with controlled morphology by physical vapor deposition. ACS Nano 9:7450–7455

[28] Kiran V, Mukherjee D, Jenjeti RN, Sampath S (2014) Active guests in the $MoS_2/MoSe_2$ host lattice: efficient hydrogen evolution using few-layer alloys of $MoS_{2(1-x)}Se_{2x}$. Nanoscale 6:12856–12863

[29] Zheng B, Chen Y, Qi F et al (2017) 3D-hierarchical $MoSe_2$ nanoarchitecture as a highly efficient electrocatalyst for hydrogen evolution. 2D Mater 4:025092

[30] Gong Q, Cheng L, Liu C et al (2015) Ultrathin $MoS_{2(1-x)}$-Se_{2x} alloy nanoflakes for electrocatalytic hydrogen evolution reaction. ACS Catal 5:2213–2219

[31] Das S, Chen HY, Penumatcha AV, Appenzeller J (2012) High performance multilayer MoS_2 transistors with scandium contacts. Nano Lett 13:100–105

[32] Susarla S, Kutana A, Hachtel JA et al (2017) Quaternary 2D transition metal dichalcogenides (TMDs) with tunable bandgap. Adv Mater 29:1702457

[33] Feng W, Zheng W, Cao W, Hu P (2014) Back gated multilayer InSe transistors with enhanced carrier mobilities via the suppression of carrier scattering from a dielectric interface. Adv Mater 26:6587–6593

[34] Chuang HJ, Chamlagain B, Koehler M et al (2016) Low-resistance 2D/2D ohmic contacts: a universal approach to high-performance WSe_2, MoS_2, and $MoSe_2$ transistors. Nano Lett 16:1896

[35] Li H, Duan X, Wu X et al (2014) Growth of alloy $MoS_{2x}Se_{2(1-x)}$ nanosheets with fully tunable chemical compositions and optical properties. J Am Chem Soc 136:3756–3759

[36] Dai T, Fan X, Ren Y et al (2018) Layer-controlled synthesis of wafer-scale $MoSe_2$ nanosheets for photodetector arrays. J Mater Sci 53:8436–8444

[37] Li Y, Wang F, Tang D et al (2018) Controlled synthesis of highly crystalline CVD-derived monolayer $MoSe_2$ and shape evolution mechanism. Mater Lett 216:261–264